Review Paper
J. Astron. Space Sci. 43(3), 129-146 (2026)
https://doi.org/10.5140/JASS.2026.43.3.129

JASS Journal of Astronomy and Space Sciences

Soviet Lunar Science in Context: From Luna to Artemis

Ulkar Karimova[1†], Yu Yi[2], Kyungguk Min[1,2]
[1]Institute for Sciences of the Universe, Chungnam National University, Daejeon 34134, Korea
[2]Department of Astronomy and Space Science, Chungnam National University, Daejeon 34134, Korea

The Soviet Luna program (1958–1976) conducted the first robotic lunar landings, rover traverses, and automated sample returns. This paper presents three major scientific outcomes from Luna missions: depth dependent regolith coarsening (70 → 130 μm) and densification (0.8 → 1.2 g/cm³), lateral geochemical gradients across mare-highland boundaries, and localized impact-generated magnetic anomalies (20–30 nT). Comparison with Apollo data shows broad agreement, with differences due to landing site geology and instrument characteristics. Operational methods from Luna remain relevant to Artemis, including specific engineering lessons from Luna 24's core drilling for South Pole drilling mechanisms.

Keywords: Soviet Luna program, Lunokhod rovers, robotic sample return, Apollo program, Artemis program, international lunar missions

1. INTRODUCTION

The Moon preserves an approximately 4.5 billion-year record of planetary accretion, impact bombardment, volcanism, and long-term surface modification, making it a fundamental target for both planetary science and future exploration. Understanding its internal structure, regolith properties, and surface processes remains essential for interpreting planetary evolution and enabling sustained human presence.

1.1 Historical Mission Context

The Apollo program and the Luna program together established the empirical foundation of modern lunar science. Apollo emphasized crewed landings at near-equatorial sites, returning 382 kg of samples and deploying geophysical instrument networks, including passive seismometers (Siddiqi 2000). In contrast, the Luna program implemented a complementary robotic strategy, targeting multiple landing sites across a broader range of latitudes, employing mobile platforms such as Lunokhod 1 and Lunokhod 2, and achieving automated sample return from both mare and highland terrains.

Key Luna milestones include Luna 2 (NASA Scientific Visualization Studio 1959), Luna 3, Luna 9 (1966), Luna 10, and Luna 16 (1970). Complementary U.S. precursor missions, including the Surveyor program and the Lunar Orbiter program, provided critical constraints on soil mechanics, surface composition, and landing site selection. Collectively, these missions produced the first detailed in situ and orbital datasets on lunar regolith structure, composition, and surface processes, although many Luna technical reports remain primarily available in Russian and contain underutilized methodological detail (Harvey 2007).

Renewed international interest has expanded the observational framework through modern orbital missions, including Kaguya, Chandrayaan-1, the Chang'e program, Lunar Reconnaissance Orbiter, Gravity Recovery and Interior Laboratory (GRAIL), and Danuri (Korea Pathfinder Lunar Orbiter, KPLO) which have refined global models of composition, gravity, polar volatiles, and operational capabilities for lunar exploration (Pieters et al. 2009; Zuber et al. 2016; Song et al. 2023).

Received 10 MAR 2026 **Revised** 02 JUN 2026 **Accepted** 08 JUN 2026
[†]**Corresponding Author**
Tel: +82-10-2197-1669, E-mail: ukgaramanka@gmail.com
ORCID: https://orcid.org/0000-0003-3396-2815

https://janss.kr pISSN: 2093-5587 eISSN: 2093-1409

1.2 Scope and Objectives

This review has three primary objectives. First, it synthesizes the principal scientific outcomes of the Luna program across four domains: regolith physical properties, surface geochemistry, geological processes, and geophysical measurements, including magnetic field investigations and laser ranging. Second, it evaluates Luna and Apollo datasets as a combined observational framework, emphasizing both instrument-dependent differences and genuine geological variability, rather than treating the programs as independent or competing efforts. Third, it identifies key engineering and scientific lessons from Luna that remain directly relevant to current and planned missions, including the Artemis program and international efforts such as Chandrayaan-3, Danuri, and forthcoming Russian missions (Luna 25–27).

Data limitations and sources. A significant fraction of the original Luna technical literature, including foundational studies (e.g., Cherkasov et al. 1968; Kocharov & Viktorov 1974; Dolginov et al. 1977), remains available primarily in Russian. Where possible, both primary sources and accessible English-language syntheses (e.g., Harvey 2007; Basilevsky 2021) are incorporated to ensure methodological clarity and completeness.

Paper organization. Section 2 presents a concise mission chronology. Section 3, forming the core of this work, organizes the scientific results into four subsections: (3.1) regolith physical properties, (3.2) surface geochemistry, (3.3) geological processes, and (3.4) geophysical investigations. Section 4 integrates Luna-derived insights with modern datasets, and Section 5 summarizes the principal conclusions.

2. HISTORICAL DEVELOPMENT AND MISSION CHRONOLOGY

The Luna program had five stages, each with its own technical and operational goals. Over time, the spacecraft got better and could work more on their own, keeping up with what U.S. lunar missions were doing (Siddiqi 2000).

2.1 Initial Reconnaissance, Impactors and Early Probes, 1958–1965

Soviet lunar missions dealt with navigation, communication, attitude control, and operation in orbit and on the surface of the Moon. Luna 1, launched in January 1959, failed to achieve its intended lunar impact trajectory and instead became the first human-made object to enter a heliocentric orbit. During its mission, it demonstrated telemetry and communication systems through the transmission of spacecraft status and scientific data to ground stations. It also demonstrated spin-stabilized attitude control and the operation of scientific instruments in deep space (Chertok 2006).

The first successful lunar impact was achieved by Luna 2, launched in September 1959 (Siddiqi 2000; Chertok 2006). Forward-mounted instruments transmitted data during terminal descent, confirming both trajectory accuracy and the predicted impact location. Measurements obtained during this phase demonstrated the absence of radiation trapping comparable to Earth's magnetosphere, implying that the Moon lacks a detectable global magnetic field. On this basis, an upper bound for the lunar magnetic moment was estimated at ~10^{-4} of terrestrial magnetic field strength (Ness et al. 1967).

Subsequent investigations have further refined our understanding of the Moon's magnetic properties. Current evidence indicates that the Moon does not possess a global magnetic field but instead exhibits localized crustal magnetic anomalies, likely remnants of an ancient dynamo or impact-related magnetization (Gattacceca et al. 2010).

Luna 3, launched in October 1959, performed a lunar flyby during which it acquired images of the lunar far side using an onboard photographic imaging system. Transmission of the image data was delayed. This delay resulted from the need to photograph the far side of the tidally locked Moon, process the exposed film onboard through development and scanning, and subsequently establish a suitable communication geometry for transmission to Earth. In addition, the limited radio transmission capability of the spacecraft resulted in weak signals and required multiple transmission attempts before usable images could be reconstructed on Earth. The returned images showed extensive previously unobserved terrain on the lunar far side (Fig. 1), providing the first global

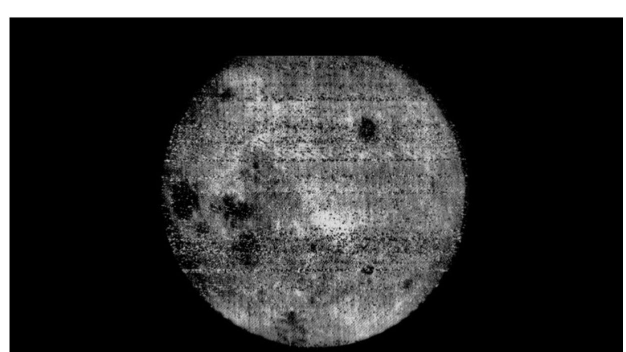

Fig. 1. First photograph of the lunar far side returned by Luna 3. Adapted from NASA Scientific Visualization Studio (1959) with public domain.

view of the Moon's far side and supporting follow-up orbital and surface exploration (Harvey 2007).

The United States' Lunar Orbiter program returned the next generation of far-side imagery between 1966 and 1967 (Bowker & Hughes 1971; see Fig. 2). Unlike the experimental film-scan system used by Luna 3, the Lunar Orbiter spacecraft employed a dual-lens photographic system with onboard film development and high-resolution scanning prior to transmission to Earth. Lunar Orbiter produced the first high-resolution photographic base maps of both the near and far sides of the Moon, supporting Apollo landing site selection.

Subsequent reconnaissance missions focused on descent control and midcourse navigation. Luna 4, launched in 1963, attempted a soft landing but failed to adjust its trajectory and passed the Moon, Luna 5-8, launched in 1965, used improved descent systems with retrorocket braking, altitude sensors, and final-stage control.

All four missions failed due to engine malfunctions, early ignition, or loss of control during landing. Telemetry included approach paths, braking performance, descent timing, and distance to the surface. Data from the missions was applied to adjust engine sequences, add sensor backups, and increase system reliability for later landings (Harvey 2007). The U.S. Ranger program (1961–1965) performed hard-landing missions to capture photographs of Apollo landing sites without soft-landing capability (Hall 1977).

2.2 Soft Landing and Surface Operations, 1966–1968

The next phase involved controlled surface operations using stationary landers. Luna 9, launched in January 1966, performed the first soft landing on the Moon (Harvey 2007).

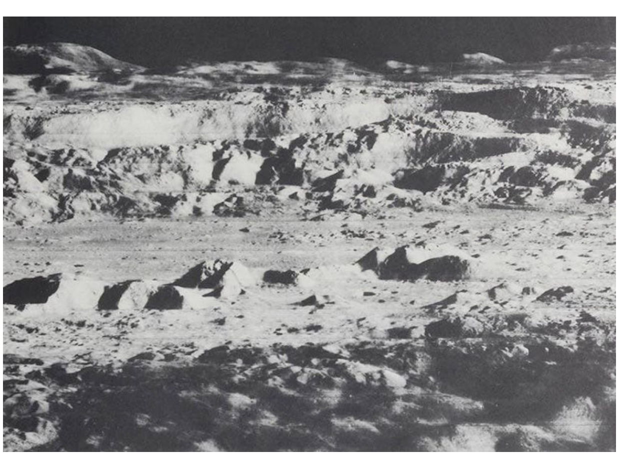

Fig. 2. Oblique photograph of the Copernicus crater taken by Lunar Orbiter 2. Adapted from Kosofsky & El-Baz (1970) with public domain.

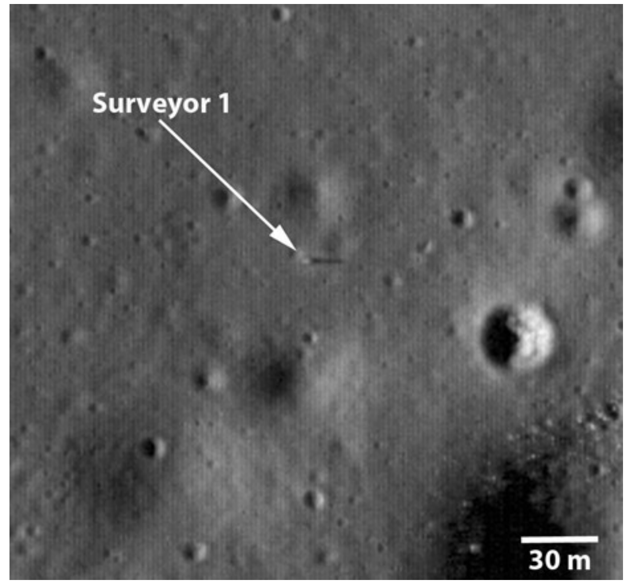

Fig. 3. Surveyor 1 on the lunar surface (Oceanus Procellarum). Adapted from NASA/JPL/GSFC/Arizona State University (2026) with public domain.

After touchdown, the lander deployed stabilizing petals and transmitted images via a mechanically scanned television system, operating until power ran out. Surveyor 1 (Fig. 3), the first U.S. soft lander, reached Oceanus Procellarum in June 1966 using a three-legged design.

Luna 13, launched in December 1966, increased surface operation capability with a larger payload and additional instruments. The spacecraft had reinforced landing structures, improved thermal insulation, and upgraded power management. Surface instruments activated automatically after landing.

The mission tested surface penetration devices, radiometric sensors, and environmental monitoring equipment under lunar gravity and vacuum. Data transmission used updated protocols from Luna 9, allowing longer operation and more efficient data return (Cherkasov et al. 1968). Operations overlapped with U.S. Surveyor missions 3–7 (1967–1968), which conducted similar experiments in soil mechanics and elemental analysis using alpha-scattering spectrometers (Christensen et al. 1967).

2.3 Orbital Science and Mapping, 1966–1974

Penetration probes, radiometric instruments, and environmental sensors were tested under lunar conditions using communication protocols developed after Luna 9 (Cherkasov et al. 1968). Similar soil and elemental studies were carried out in the U.S. Surveyor Program with Surveyor 3–Surveyor 7 (Christensen et al. 1967). Orbital observations began with Luna 10, the first lunar satellite (Vinogradov et al. 1966), while Lunar Orbiter 1 imaged candidate Apollo landing areas (Bowker & Hughes 1971). Later missions improved mapping and measurements, including imaging from Luna 12, gravity tracking by Luna 14, and long-term observations from Luna 19 and Luna 22 (Siddiqi 2000; Harvey 2007).

2.4 Automated Sample Return, 1970–1976

Sample-return missions were automated and required precise lunar landings, subsurface sampling, ascent from the Moon, and controlled return to Earth. Luna 15, launched in July 1969, attempted an autonomous landing but struck the surface, showing the challenge of achieving accurate descent without real-time control (Siddiqi 2000). Its launch coincided with the Apollo 11 mission, when the first human touched the Lunar ground. Luna 15 represented the first sample return attempt, crashing two days after Apollo 11's landing (Siddiqi 2000).

Luna 16, launched in September 1970, completed the first robotic sample return from another planetary body. The mission showed that fully automated planetary sample return was feasible (Vinogradov 1971).

Luna 16 followed Apollo 11 and 12, providing a robotic alternative to crewed sample return (Heiken et al. 1991). The landing site was a smooth lunar mare, selected for drilling and sampling, located near but separate from previous Apollo sites (see Fig. 4.).

Luna 20, launched in February 1972, landed in highland terrain and performed automated sample return using modified landing and drilling systems suited for uneven surfaces. The missions confirmed that sample-return systems worked across different terrain (Harvey 2007).

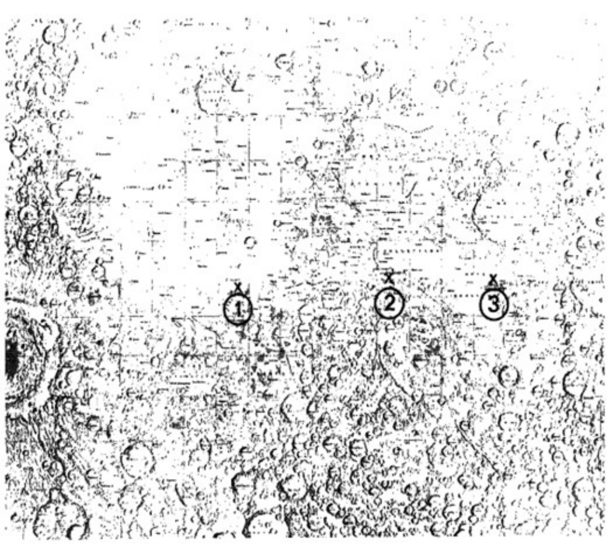

Fig. 4. Map of the Moon showing: (1) the Apollo 12 landing site; (2) the Apollo 11 landing site; and the Luna 16 landing site. Adapted from Vinogradov (1971) with permission of the author.

Luna 23 landed in October 1974 but suffered mechanical damage and could not collect samples. Luna 24, launched in August 1976, used a redesigned drill to retrieve a deep core. Sample-return operations showed that drilling, containment, ascent, and recovery systems were reliable, marking the end of the Soviet robotic lunar sample program (Heiken et al. 1991). These missions followed U.S. lunar landings and kept in situ lunar studies going into the mid-1970s (Harvey 2007).

2.5 Mobile Surface Exploration, The Lunokhod Program

The Lunokhod program brought mobile robotic exploration to the Moon. Lunokhod 1, delivered by Luna 17 in November 1970 to Mare Imbrium, had an eight-wheeled chassis with independent motors and suspension for rough terrain (see Fig. 5).

Solar panels supplied power during the day, while internal radioisotope heaters worked at night. Instruments included panoramic cameras, surface analyzers, particle detectors, and a laser retroreflector for geodetic measurements.

Rover movements were controlled from Earth in short steps, with images and telemetry sent back after each move. Navigation routines, backup mobility systems, and continuous terrain checks kept operations running. Lunokhod 1 worked at the same time as the Apollo Lunar Roving Vehicles gave astronauts mobility on crewed missions (Basilevsky 2021).

Lunokhod 2 arrived at Le Monnier crater in January 1973 on Luna 21. The rover had improved mobility, better cameras, and more instruments for measuring the environment. It included a magnetometer, navigation cameras, and compartments for scientific equipment, allowing longer and more detailed surface operations (Fig. 6).

Operations covered varied terrain and demonstrated long-range performance under repeated thermal cycles. Mission termination occurred due to degradation of thermal control caused by surface contamination, showing sensitivity of radiator systems to fine particulate material. Lunokhod 2 remained the only active robotic platform on the lunar surface from 1973 until the end of the decade (Harvey 2007).

The rover's traverses and interactions with terrain are summarized in Fig. 7 (Basilevsky 2021), which shows the route of Lunokhod 2 and labeled craters named in honor

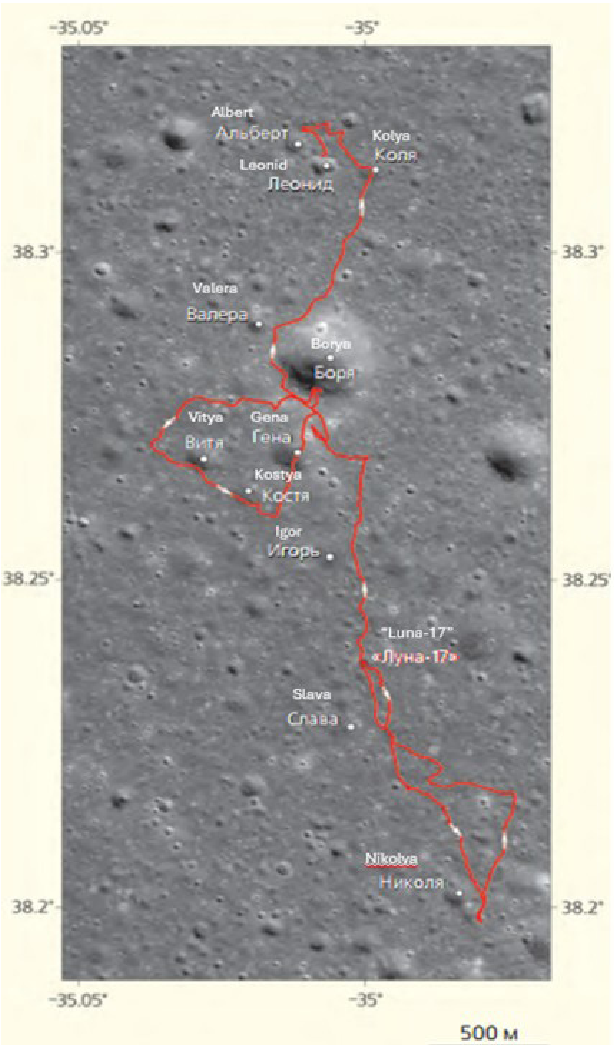

Fig. 5. Route of Lunokhod 1 and crater names corresponding to members of the rover team (as they referred to one another). Arrows along the route indicate the direction of rover movement. The image is a mosaic created from Lunar Reconnaissance Orbiter LROC NAC (Narrow Angle Camera) images. Crater names transliterated from Russian into English by the authors. LROC NAC, Lunar Reconnaissance Orbiter Camera Narrow Angle Camera. Adapted from Basilevsky (2021) with permission of the author, with data from Karachevtseva et al. (2013).

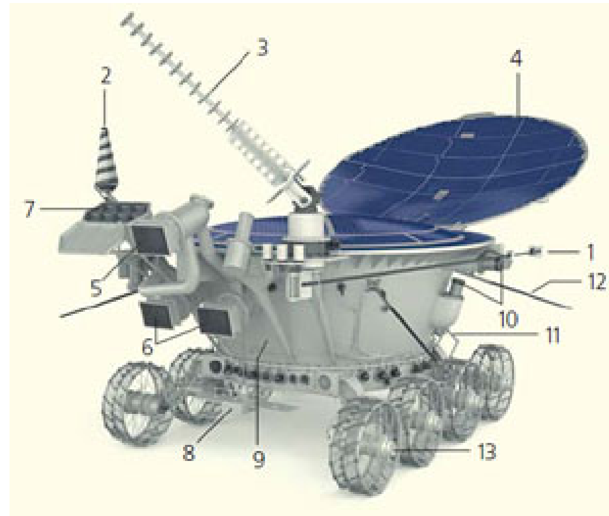

Fig. 6. Diagram of Lunokhod-2. (1) Magnetometer, (2) Omnidirectional antenna, (3) Directional antenna, (4) Solar panel, (5) Upper navigation TV camera, (6) Lower navigation TV cameras, (7) Corner reflector, (8) Remote equipment block "RIFMA", (9) Hermetic container with scientific instruments, (10) Panoramic TV cameras, (11) Mobility assessment device – penetrometer (PrOP/ПРОП, Penetrometer–Passability/Penetration–Passability device), (12) Whip antenna, (13) Wheel motor. RIFMA, X-ray fluorescence spectrometer. Adapted from Basilevsky (2021) with permission of the author, with data from Karachevtseva et al. (2013). Additional instrument details available in Harvey (2007) and Siddiqi (2000).

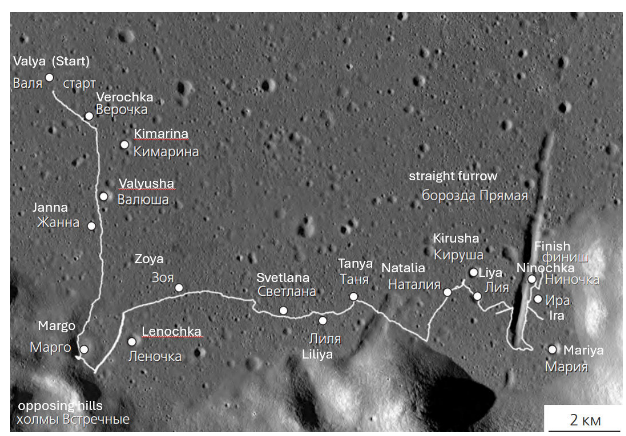

Fig. 7. Route of Lunokhod 2, showing labeled craters named in honor of women who contributed to rover operations and data analysis. Mosaic compiled from LROC NAC images. Crater names transliterated from Russian into English by the authors. LROC NAC, Lunar Reconnaissance Orbiter Camera Narrow Angle Camera. Adapted from Basilevsky (2021) with permission of the author, with data from Karachevtseva et al. (2013).

of women who contributed to rover operations and data analysis. Maneuvering in the crater with the solar panel cover uncovered, Lunokhod-2 snagged it on the inner slope of the crater.

Soil accumulated on the panel's surface, which was immediately noticed from Earth due to a decrease in charge current. At the end of the fourth lunar day, as the rover went into the night, the cover had to be closed; otherwise, it could have frozen overnight, and the soil (which is an excellent thermal insulator) covered the radiator. On the next (fifth) lunar day, the radiator, covered with lunar soil, poorly radiated heat into space. On May 10, the rover overheated and no longer responded to communications.

Rover operations involved coordination among drivers, navigators, engineers, and scientists. Commands were executed incrementally based on sequential analysis of images, allowing control under communication delays. TV panoramas of the Lunokhod 2 work area illustrate the

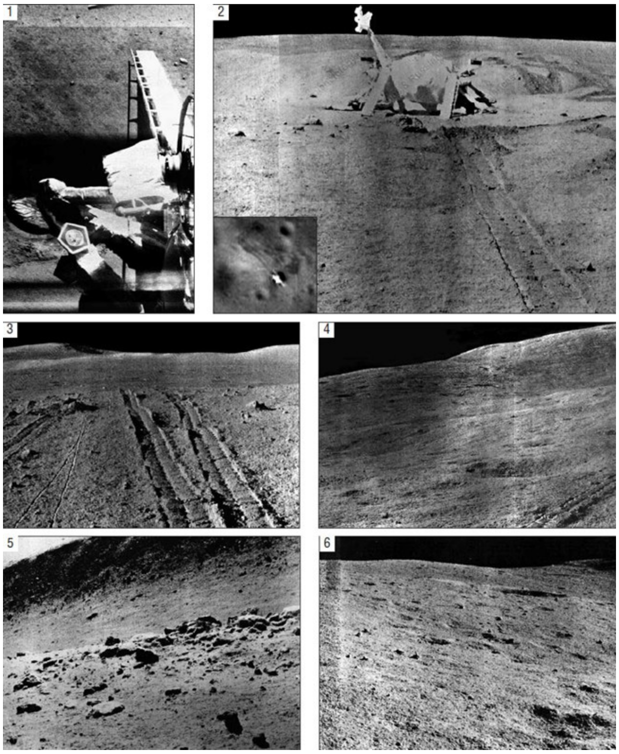

Fig. 8. Landscapes of the Lunokhod-2 work area. Fragments of TV panoramas captured by the rover's cameras. (1) Panorama from the vertical camera before the rover descended from the landing platform, with an arrow indicating a bas-relief of Lenin; (2) Landing platform after rover descent; inset (left) shows Luna 21 in LROC NAC M122007650LE image; (3) Plain at the base of Le Monnier crater with rover wheel tracks; (4) Landscape within the Meeting Hills; (5) Scatter of rocks on the western edge of the Direct Trench depression; (6) Landscape on the morning of the fifth lunar day, immediately prior to the session when Lunokhod2 ceased responding to Earth commands. LROC NAC, Lunar Reconnaissance Orbiter Camera Narrow Angle Camera. Adapted from Basilevsky (2021) with permission of the author.

operational environment (Fig. 8). Data from Lunokhod missions demonstrated the feasibility of long-duration robotic surface traversal and provided operational procedures later applied to other planetary rover programs. For comparison with modern rover imagery see Fong et al. (2010).

3. SCIENTIFIC OUTCOMES AND CONTRIBUTIONS

Multidisciplinary data from Soviet lunar missions established first-order constraints on fundamental lunar properties and processes. The following sections group the main results by scientific domain.

3.1 Regolith Physical Properties and Mechanical Behavior

Systematic characterization of lunar regolith physical and mechanical properties represented one of the most consequential scientific contributions of Soviet surface exploration. Prior to direct surface interaction, large uncertainty surrounded near surface strength, density, and load bearing behavior, with some pre mission hypotheses proposing extremely weak or deeply unconsolidated surface layers.

Measurements obtained by Luna 13, as reported by Cherkasov et al., indicate that a mechanical penetrometer deployed at Mare Cognitum recorded an average bulk density of 0.8 ± 0.1 g/cm^3 and a bearing strength of 0.1–1.0 kg/cm^2 within the upper ~20 cm of the regolith. However, this value represents a depth-weighted response dominated by the very shallow subsurface, effectively corresponding to the uppermost few centimeters (~1–5 cm), where porosity is estimated to be on the order of 60%–70%.

For comparison, Apollo drilling and core analyses summarized by Carrier et al. demonstrate a systematic increase in density with depth, from ~0.5 g/cm^3 at the immediate surface to ~1.6 g/cm^3 at depths approaching 2 m. Higher-resolution core data further reveal a pronounced vertical gradient in porosity and density, with values of ~50%–60% (≈0.9 g/cm^3) at 0–5 cm, decreasing to ~40%–45% (≈1.3 g/cm^3) at 5–20 cm, and to ~35%–40% (≈1.5 g/cm^3) at 20–50 cm. The apparent discrepancy between Luna 13 estimates and Apollo-derived densities (1.3 ± 0.2 g/cm^3 at 1–15 cm) arises primarily from differences in measurement methodology, specifically, penetration resistance versus direct mass–volume determination. Nevertheless, both datasets consistently indicate that the uppermost regolith is highly porous (> 50%), forming a mechanically weak and compressible surface layer.

The penetrometer on Luna 13 operated through incremental loading during controlled insertion, with resistance inferred from load–depth relationships. These measurements demonstrated that, despite its рыхлый structure, the near-surface regolith possesses sufficient bearing capacity to support landed spacecraft, thereby resolving early uncertainties regarding the presence of deep, low-strength dust deposits. The derived density and strength parameters subsequently provided key constraints for impact cratering models, in which porosity and cohesion strongly influence excavation depth, ejecta velocity, and crater morphology.

Spatial extension of these point measurements was achieved through rover-based investigations conducted by Lunokhod 1 and Lunokhod 2. Both platforms were equipped with the Penetrometer–Passability/Penetration–Passability device (PrOP) penetrometer, enabling measurements of static penetration resistance and rotational shear resistance across diverse terrain types. Static penetration data provided estimates of compressive strength and bearing capacity, whereas rotational measurements constrained shear strength associated with interparticle friction and grain interlocking. Collectively, these in situ observations significantly refined the mechanical characterization of lunar regolith beyond the limitations of single-point lander measurements.

Rocks encountered along the traverses of Lunokhod 1 and Lunokhod 2 differ in their primary shape, reflecting variations in fracturing (Fig. 9, column 1), which are controlled, in part, by the nature of the original rock and the degree of modification of that primary form (Fig. 9, columns 2 and 3). In images of modified rocks, rounded depressions are visible, which are most likely the result of meteoroid impacts. Diurnal temperature variations, reaching approximately 250°C–300°C, also contribute to the progressive breakdown of exposed surface rocks.

With respect to thermal fatigue, diurnal temperature variations, with amplitudes of $\Delta T \approx 280$ K, may play a role in rock disintegration, but their effectiveness remains debated. Impact bombardment is widely recognized as the dominant mechanism of rock fragmentation on the lunar surface (Basilevsky 1974, 2021). Thermal fatigue, if effective at all, likely acts as a secondary process, enhancing the breakdown of rocks already weakened by microcracks from impacts.

Analysis of more than five hundred penetrometer measurements collected by Lunokhod 1 documented substantial spatial variability in regolith mechanical response, with penetration resistance values ranging from approximately 0.2 to 2.5 kilograms per square centimeter (Basilevsky 2021).

Mapping of measured values along rover traverses indicated systematic association between higher resistance

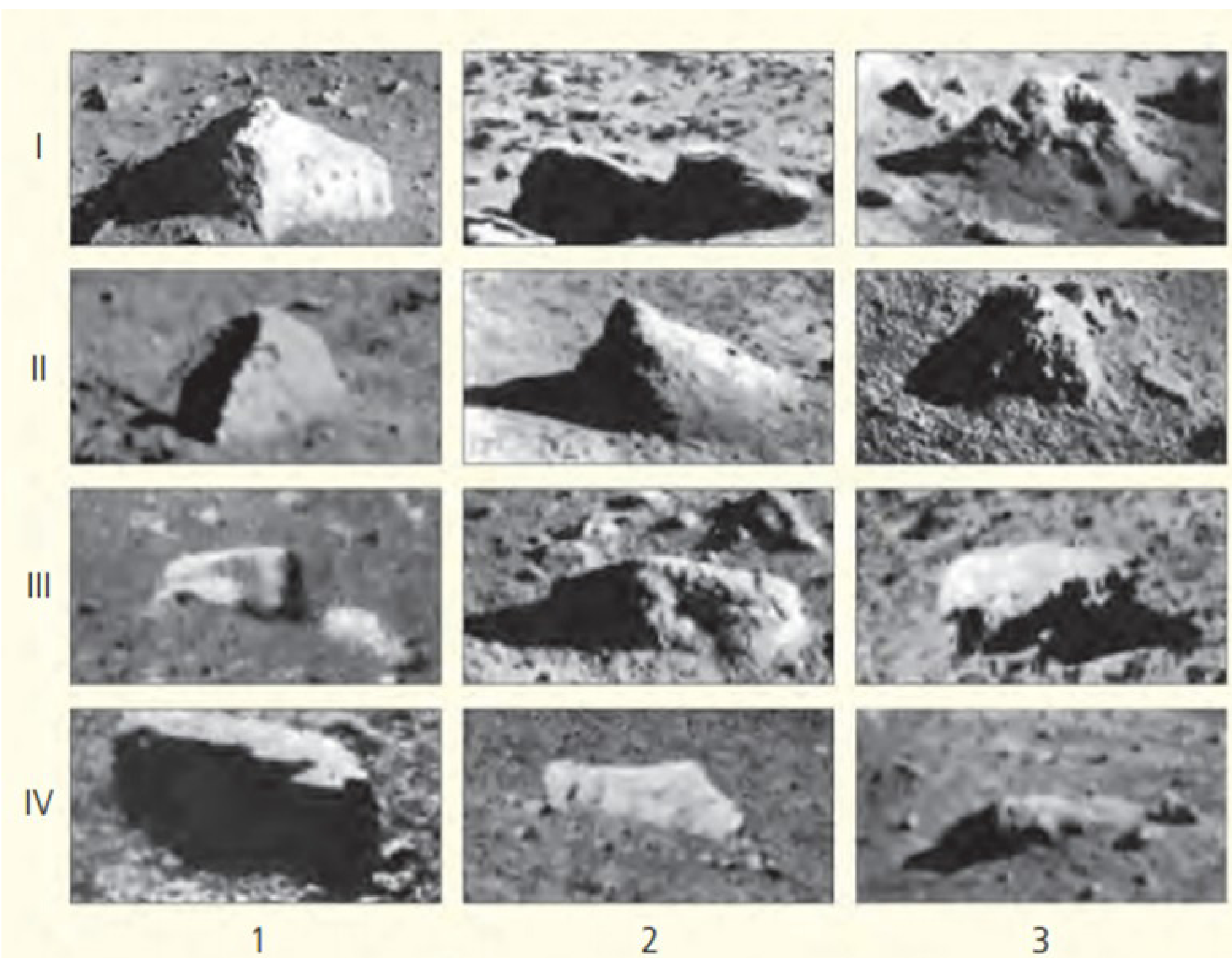

Fig. 9. Rocks ranging in size from a few decimeters to several meters. Different types are distinguished according to their original shape (vertical axis) and the degree of modification by surface processes (horizontal axis). Fragments of TV panoramas from Lunokhod1 and 2. Adapted from Basilevsky (2021) with permission of the author. See also Heiken et al. (1991) and McKay et al. (1991) for complementary morphological descriptions.

values and surface textures characterized by increased rock abundance, rougher microtopography, and morphological indicators of advanced regolith maturation.

Rock samples and geophysical readings were collected at six Apollo equatorial sites. Luna missions reached other areas using orbiters, landers, and sample-return vehicles (Siddiqi 2000).

Most Luna mission documentation is found in technical reports, conference proceedings, and Russian-language publications, with limited availability in Western literature (Harvey 2007). Review of source material clarifies mission procedures, instrumentation, and scientific output.

Operational methods developed under Luna remain relevant for analysis of orbital datasets and planning of future missions. Comparison of Luna and Apollo measurements indicates generally consistent findings, with differences mainly related to landing-site location. Combined records provide a basis for studies of lunar geology, regolith mechanics, and surface processes.

3.2 Surface Geochemistry and Compositional Diversity

Measurements of chemical composition from Luna missions included multiple sites; earlier observations and a small number of returned samples left many regions unexamined. Surface operations addressed this limitation using instruments capable of repeated measurements along rover traverses. Lunokhod rovers carried the RIFMA X-ray fluorescence (XRF) spectrometer. RIFMA's energy resolution was ~400 eV at 5.9 keV (Fe-55 source), with detection limits of ~0.1 wt% for major elements. Crosscalibration with Apollo XRF data shows systematic offsets of ± 10% for Al and Si. Sealed radioactive sources irradiated the soil, and emitted X-rays were detected with thin-window proportional counters. During Lunokhod 2 operations at Le Monnier crater, RIFMA measured elemental abundances in the upper few millimeters of regolith. Aluminum averaged 9 ± 1 wt.% and iron 6 ± 0.6 wt.%, with local variations reflecting mixing with highland material. Data from Lunokhod traverses provided geochemical coverage of previously unmeasured areas and allowed comparison with Apollo samples, showing lateral variation in surface composition (Kocharov & Viktorov 1974).

Lunokhod 1 made more than twenty-five compositional measurements along its traverse though later evaluations showed that only a subset yielded statistically robust results (Basilevsky 2021).

Measurements showed basaltic compositions typical of lunar maria, with iron oxide concentrations from approximately sixteen to nineteen weight percent and titanium dioxide from four to five weight percent (Basilevsky 2021).

Measured values matched orbital spectral classifications of high-titanium mare basalts and showed variation between sampling points separated by hundreds of meters. Signal acquisition was stabilized by direct surface contact, with integration times ranging from minutes up to tens of minutes based on surface roughness and counting rates (Basilevsky 2021).

Regolith from the Sea of Plenty is dark gray to black and contains both rounded, melted grains and angular fragments (see Fig. 10). Most particles are about 0.1 mm in size, and grain sizes follow a power-law distribution typical of broken material.

Polarization measurements from Luna 16 showed a phase curve minimum at ~15° phase angle, consistent with finegrained (40–70 μm) agglutinates (Vinogradov 1971). Geometric albedo of the sampled regolith is ~0.07; Bond albedo ~0.12. The 35 cm column can be divided into five main zones based on physical properties.

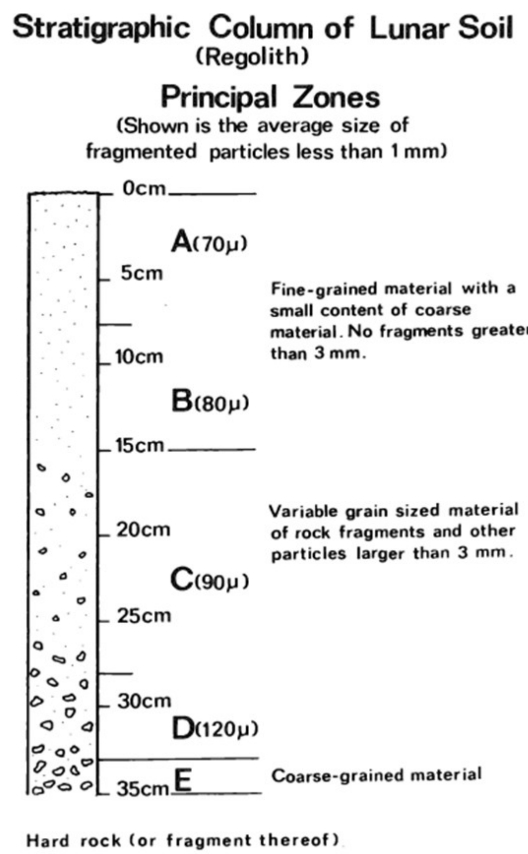

Fig. 10. Vertical Structure of Regolith in the Sea of Plenty. The 35 cm-thick regolith consists of five strata labeled A through E, with median grain size increasing with depth and intermittent rock fragments above 3 mm. Adapted from Vinogradov (1971) with permission of author.

- Zones A and B (0–15 cm): Upper layers consist primarily of fine-grained material. Zone A has a median grain size of 70 μ, increasing to 80 μ in Zone B. Zones are notable for a low content of coarse material and a total absence of fragments exceeding 3 mm.
- Zones C and D (15–33 cm): Middle layers exhibit higher variability in grain size. Median grain sizes increase from 90 μ (Zone C) to 120 μ (Zone D). Zones show low content of coarse material and lack fragments larger than 3 mm unlike the upper layers.
- Zone E (33–35 cm): The base of the sampled column consists of the coarsest material encountered.

Measurements reached a depth of 35 cm. Regolith thickness in the area was estimated to be between 0.5 and 1 m above bedrock or large fragments. Geochemical measurements obtained at the Apollo 12 and Apollo 15 landing sites revealed systematic variations in elemental abundance ratios between the two locations. Composition across Mare Imbrium was heterogeneous, with titanium and iron changing across the plains, which suggests multiple lava flows from different sources or different degrees of partial melting. Lunokhod 2 recorded compositional measurements across several geological regions. On the basaltic plains of Le Monnier crater and toward the highland rim, iron oxide decreased from 7.5 to 4.0 wt.% Fe over eight kilometers, while aluminum oxide increased from 9 to 11.5 wt.% Al_2O_3 (Kocharov & Viktorov 1974). Gradual variations indicate mixing of mare basalt with aluminum-rich anorthosite rather than sharp lithological contacts.

Compositional variations reflect highland material mixed into mare regolith by impacts. Data show fine-grained material traveled several kilometers from ejecta of distant impacts and surface disturbance processes (Szalay et al. 2019). Data help estimate regolith mixing and variation across the surface.

Returned samples and surface measurements show lunar composition at multiple sites. Luna 16 returned approximately 100 g of material from Mare Fecunditatis, primarily low-titanium mare basalt with TiO_2 contents of 2–3.4 wt.%, lower than at the Apollo 11 and 12 sites (Vinogradov 1971). Trace element and rare earth analyses indicate a distinct magmatic source consistent with nearby regions. Luna 20 samples from highland terrain are dominated by anorthosite containing 75%–90% plagioclase feldspar (Harvey 2007) and include polymict impact breccias with fragments of multiple rock types within a fine-grained matrix; mineral deformation and shock features record prolonged impact processing. A two-meter core was returned from Mare Crisium by Luna 24, containing stratified layers with variations in grain size, mineral composition, and maturity inferred from agglutinate content (Heiken et al. 1991). Some layers differed from local mare basalts because of material transported by distal impacts. Core analysis indicated regolith formation through surface mixing and deposition of ejecta, and measurements conducted at the surface and in the laboratory indicated compositional differences both laterally and with depth. Geochemical results from the Luna missions formed an important basis for resource assessment, geological mapping, and calibration of orbital datasets.

3.3 Geological Processes and Surface Evolution

Meter- to submeter-scale views of the lunar surface were obtained across both mare and cratered terrains during the Luna 9 and Luna 13 missions (Cherkasov et al. 1968). Surface rocks ranged from a few centimeters to more than a meter in size and were mostly angular or subangular, following a power-law distribution typical of impact debris. Some larger rocks were partially buried, indicating earlier impact events, while ejecta around small craters formed clusters of blocks. Terrain slopes remained largely stable. Rover operations extended the surveyed area by several kilometers, and repeated imaging under different illumination conditions supported detailed mapping of surface features. Measurements of surface roughness, slope variation, and block distribution documented processes responsible for regolith modification over time (Basilevsky 1974). Small impact craters, from 0.1 m to 2 km in diameter, were examined and classified according to rim sharpness, ejecta preservation, interior infilling, and evidence of wall slumping. Well-preserved craters exhibited sharp rims and continuous ejecta, moderately degraded craters showed partial rim and ejecta erosion, and highly degraded craters displayed subdued rims and infilled interiors (Basilevsky 1974).

Crater types along rover routes were used to estimate relative surface exposure ages. Preservation states were compared with crater populations and radiometrically dated Apollo samples, allowing relative age dating to be applied to regions without returned samples (Basilevsky 1974). Morphological dating based on the degradation of small craters has since been applied to other planetary bodies, including Mercury, Mars, and asteroids.

3.3.1 Character of the Evolution of Small Craters

Small lunar craters, typically ranging from 1 m to 2 km in diameter, are predominantly bowl-shaped. While rare varieties such as flat-bottomed or concentric craters exist, these deviations usually indicate a double-layered target structure consisting of unconsolidated regolith over a hard-rock substrate (see remarks on Fig. 11(a) and (b) below).

Table 1 shows that craters form a continuous morphological series divided into five classes (A, AB, B, BC, and C) based on the sharpness of their relief. For craters of the same diameter, this sequence reflects an increase in age as the morphology becomes more degraded:

- Morphological Maturity: Class A craters are defined as the "freshest" or youngest, while Class C represents the most "mature" or ancient stage of development.
- Population Dynamics: In non-equilibrium populations, such as those found on lunar maria, there is a higher proportion of steeply sloping forms (Classes A and B). Conversely, in equilibrium populations, gently sloping craters (BC and C) make up the majority.
- Degradation Factors: The transition from a "fresh" Class A profile to a "mature" Class C profile is driven by the slow process of lunar erosion. Craters of classes BC and C with diameters exceeding 1 km are extremely rare on maria surfaces, suggesting that the degree of preservation is a function of both age and initial size.

Lunokhod 2 observed a straight tectonic feature called the Direct Trench in Le Monnier crater. Close-up images showed an area about 100 meters wide at the edge of the trench, where fine regolith was reduced. Exposed surfaces had tightly packed rock fragments forming a continuous

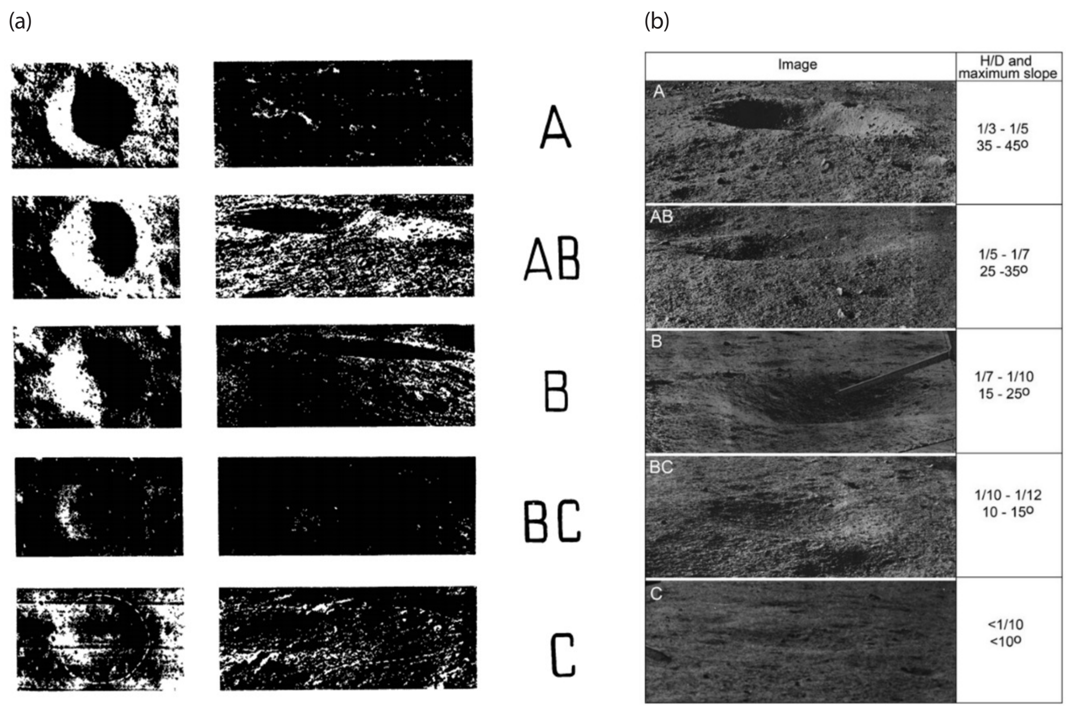

Fig. 11. Morphological classification of small lunar craters. (a) Original photographs of craters belonging to different morphological classes (A through C), illustrating the evolutionary sequence of small lunar craters. The left column shows craters 400–500 m in diameter (Lunar Orbiter II/III); the right column shows craters 3–5 m in diameter (Lunokhod 1/2). Solar angles are 20°–30°. These images have poor resolution and do not clearly convey the quantitative classification criteria. (b) The same morphological classification presented in a clear, quantitative tabular format, showing the depth-to-diameter (H/D) ratio and maximum inner slope angle for each class. This table is added for clarity because the original photographs in (a) are not sufficiently legible. Adapted from Basilevsky (1974), with data from Basilevsky et al. (2015).

Table 1. Morphological classes Lunar craters (A–C)

Class	Geomorphological characteristics	Relative depth	Max.Inner slope angle
A	Very steep slopes; clearly defined rim; prominent blocky ejecta zone.	1/3–1/5	35°–45°
AB	Steep slopes; sharply defined, slightly flattened rim; discernable ejecta zone with common blocks.	1/5–1/7	25°–35°
B	Moderately steep slopes; smoothed rim outlines; blocky material infrequent except on the rim.	1/7–1/10	15°– 25°
BC	Gently sloping; poorly pronounced rim; outer surface nearly indistinguishable from inter-crater space.	1/10–1/12	10°–15°
C	Very gently sloping; minimal relief; rim and crater surface differ very little from surrounding terrain.	< 1/12	< 10°

Data from Basilevsky (1974).

layer rather than separate blocks in the soil (Basilevsky 1974).

The arrangement of fragments, continuous surfaces, and smooth transition into regolith-covered areas suggest that fine material was removed rather than not deposited. Because there is no atmosphere or water, seismic shaking from tectonic activity or distant impacts redistributes regolith. However, recent studies emphasize electrostatic dust levitation driven by solar UV and plasma interactions as an additional transport mechanism (Severny et al. 1975). In polar regions, electrostatic lofting may dominate over seismic effects for particles < 100 μm (Hartzell 2019). The depth of regolith removal and the area affected allow estimation of downslope movement of fine material at 0.1 to 1.0 millimeters per year, assuming occasional seismic events over long periods (Basilevsky 1974).

3.4 Geophysical Investigations

Magnetic Field Investigations of Dolginov et al. 1977 indicate that Lunokhod 2 utilized a three-component fluxgate magnetometer to perform a surface survey in Le Monnier Bay. The mission identified a mean magnetic field of 20–30 gammas (nanotesla), with local anomalies of 10–15 gammas specifically confined to craters exceeding 50 m in diameter. The variations were observed over distances of tens to hundreds of meters, suggesting that the magnetized sources are limited to shallow crustal layers.

Luna missions provided data from which crustal structure could be inferred. For example, tracking of Luna 10 and Luna 14 orbiters gave gravimetric constraints on crustal thickness (Vinogradov et al. 1966). The term “internal structure” here refers to crustal layering and upper mantle density, not full coretosurface characterization. Orbital motion of the Moon (e.g., recession rate) was not measured by Luna missions; it is derived from lunar laser ranging using retroreflectors on Lunokhod rovers (discussed later in this section). Instruments on the surface recorded magnetic fields, local gravity effects, and surface movement in areas not accessible to orbiters.

Fig. 12 displays the magnetograms of the horizontal (H) and vertical (Z) field components. The angular dimensions of the crater profiles are provided to scale, illustrating that magnetic anomalies are linked to the physical boundaries (edges) of the craters (Dolginov et al. 1977).

- Total Field Magnitude (T): Contrary to topographic interpretations, the “T” values represent the scalar magnitude of the magnetic field. Variations in T of up to 10 gammas occur over craters, with the most pronounced changes localized at the crater edges.
- Vertical Component (Z): This component exhibits distinct fluctuations ranging from –10 to +40 gammas. The behavior of Z serves as the primary indicator for classifying the magnetic signature of a crater.
- Horizontal Component (H): This line tracks the horizontal intensity, with values ranging from 2–3 to 30 gammas. Significant deviations in H are often mirrored by the Z component, depending on the signature type.

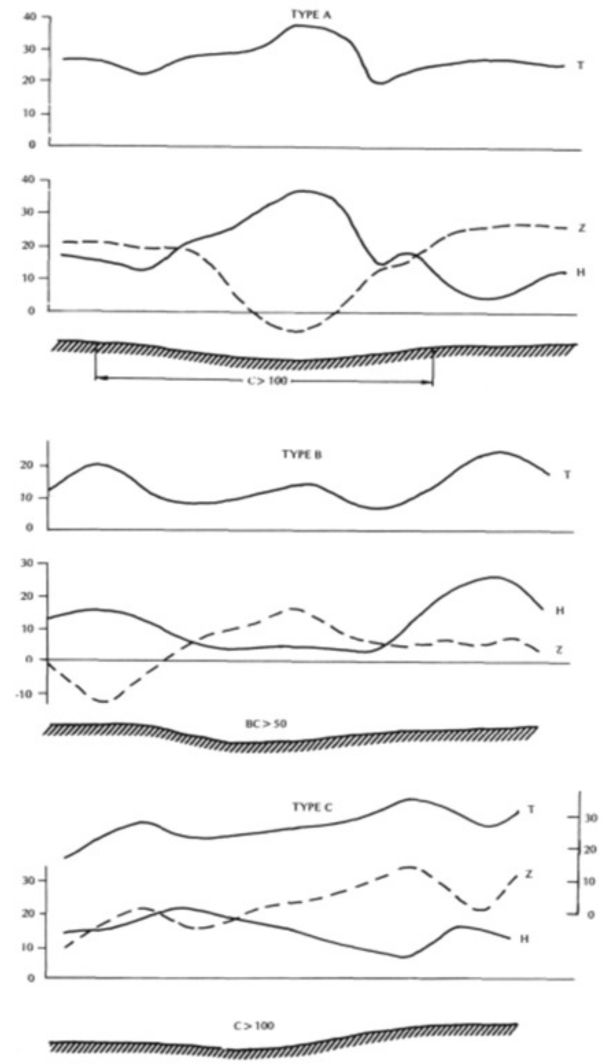

Fig. 12. Relationship between crater degradation state and magnetic signature. Topographic relief (T). Adapted from Dolginov et al. (1977) with permission of author.

3.4.1 Classification of Magnetic Anomalies

The study categorizes the relationship between the field and the crater morphology into three distinct types, rather than evolutionary stages:

- Type A: Characterized by a minimum in the Z component and a maximum in the H component directly above the center of the crater.
- Type B: Characterized by a maximum in the Z component and a minimum in the H component above the center.
- Type C: Observed primarily in crater chains; characterized by a maximum in Z and a minimum in H specifically located over the crater edge.

The data indicate that smaller craters, with diameters under 50 m, produce effects below the detectable limit. For larger, well-preserved craters (classes, classified as very sharp (VS) and sharp (S) in Basilevsky's (1974) morphological scheme) with slopes up to 7°, the observed anomalies imply that impacts either erased preexisting local magnetization or generated new thermoremanent magnetization. This confinement of anomalies to craters provides proof of a direct link between lunar surface morphology and localized crustal magnetism.

Interpretation of anomaly geometry and intensity supported formation through shock remanent magnetization acquired during hypervelocity impacts into magnetized target materials or transient impact generated magnetic fields. Experiments on shocked lunar analog materials demonstrate efficient remanent magnetization under pressures comparable to impact conditions. Evidence indicates impact-generated magnetization (Gattacceca et al. 2010). Magnetometer data also contributed constraints on the strength and temporal persistence of any ancient lunar dynamo by limiting the intensity of ambient magnetic fields required during magnetization events. Paleofield strengths estimated from anomaly magnitudes matched values from laboratory analysis of returned lunar samples, consistent with a core magnetic field active during the Moon's first billion years.

Laser retroreflector arrays on Lunokhod 1 and Lunokhod 2, installed by French teams, increased geodetic coverage and advanced tests of fundamental physics. Corner cube prisms returned laser pulses to Earth with minimal angular dispersion. The Lunokhod 1 reflector functioned for a limited interval after the mission. Identification of the rover location in 2010 by Lunar Reconnaissance Orbiter imagery restored opportunity for additional ranging experiments (Murphy et al. 2011). Renewed ranging extended baseline coverage and measurement sensitivity for rotational and tidal parameters.

Decades of lunar laser ranging recorded variations in Earth Moon distance, long term orbital evolution, and rotational motion. Analysis indicated a mean lunar recession rate near 3.82 cm per year, attributed mainly to tidal dissipation within Earth oceans and interior (Williams et al. 2001). Changes in the Moon's recession from Earth reflect differences in how energy is lost at different frequencies and the slow evolution of the Earth–Moon system. Small, regular variations in lunar rotation suggest that the mantle and core are partially decoupled, indicating a fluid outer core. Models of the Moon's rotation point to a core radius of about 350 km made of low-viscosity liquid metal, possibly containing sulfur or other light elements (Weber et al. 2011).

3.5 Lunar Environment and Astronomical Observations

Forward scattering of sunlight above the lunar surface indicates the presence of fine dust particles. Estimated grain sizes range from submicron to micron scale, consistent with lunar regolith. A scattering layer reaching tens of meters above the surface is indicated by radiometric measurements. Surveyor images recorded dust rising near the terminator after sunset (Rennilson & Criswell 1974), and Apollo limb observations confirmed elevated dust under appropriate lighting.

In addition to dust lofted by meteoroid impacts and lander exhaust, electrostatic dust levitation is now recognized as a persistent environmental process. Solar UV radiation and plasma interactions charge lunar regolith particles, leading to spontaneous lofting and horizontal transport even in the absence of mechanical disturbance (Severny et al. 1975). Evidence from Lunokhod2's horizon brightness enhancement (Severny et al. 1975) may be partly attributable to this mechanism. Electrostatic dust transport is particularly relevant for polar regions and for future missions such as Artemis, where levitated dust can contaminate optics, solar panels, and thermal radiators.

The Moon's surface is blanketed by a loose regolith layer that controls how the terrain interacts with vehicles and other mobile loads (Basilevsky et al. 2021). Under undisturbed conditions, this results in sinkage depths of 9–49 mm, corresponding to soil compressive strengths of 9.8–23.4 kPa. When a lander descends, its engine exhaust blows away the upper loose layer, leaving a denser, more compacted surface. Reduced track depths of 9–12 mm and brightened halos around landing platforms indicate modification by gas dynamic erosion.

The lunar environment is characterized by large temperature variations and exposure to high-energy radiation. The reports on surface temperatures ranging from −90℃ to +150℃, with values of +120℃ measured during the fourth lunar noon. The environment combines high vacuum with continuous exposure to corpuscular flows of cosmic rays. Energy regions measured are unattainable on Earth owing to the Moon's lack of atmospheric shielding and intrinsic magnetosphere. X-ray radiation contributes additional energy, with quanta in the 2,000–10,000 eV range. Interacting thermal, mechanical, and radiation factors create a lunar surface that is abrasive, experiences extreme temperature swings, and is exposed to continuous radiation.

3.6 Competitive Context and Methodological Divergence

Luna robotic missions operated during the Cold War at the same time as Apollo crewed missions. Apollo missions had astronauts observe the surface, take samples, and set up instruments. Surveyor landers and Lunar Orbiter spacecraft gathered data before crewed landings. Luna missions covered extensive surface regions, in contrast to Apollo missions, which focused on chosen sites and added data that supported Luna observations.

3.7 Comparative Outcomes: Apollo Contributions and Soviet Counterparts'

Data from Apollo missions covered multiple areas of lunar science and supplemented results from Luna missions. Table 2 compares selected measurements from the two programs. Published studies provide the values. The table lists chemical composition, regolith density, magnetic fields, and dust movement. Individual entries reflect specific studies, with other sources reporting broader ranges or alternative values.

3.8 Cross-Program Observational Comparison

Analysis of differences: The numerical differences between Luna and Apollo measurements arise from a combination of instrument characteristics and genuine local geological variations. For regolith density, the lower Luna value (0.8 ± 0.1 g/cm^3) reflects measurement of the uppermost 1–5 cm by a mechanical penetrometer, whereas Apollo drill cores integrated over 30–60 cm depth, capturing denser material at depth. The density gradient observed in Apollo cores (surface ~0.5 g/cm^3 increasing to ~1.6 g/cm^3 at 2 m) indicates that both datasets are consistent when depth is considered. For titanium content, the difference (Luna lowTi vs. Apollo highTi) is a real geological variation: Luna 16/24 landed in eastern maria (Mare Fecunditatis and Mare Crisium) underlain by lowTi basalts, while Apollo 11/17 sampled highTi basalts from western maria (Mare Tranquillitatis and Mare Imbrium). Magnetic field differences arise from spatial scale: Lunokhod 2 measured local, craterconfined anomalies at meter scale (20–30 nT), while Apollo subsatellites mapped regional orbital fields (< 1 nT). The larger surface fields at Apollo landing sites (e.g., 232 nT at Apollo 16) reflect local crustal magnetization, not instrument error. Thus, the table entries reflect both methodological differences and true lunar heterogeneity.

Surveyor landers measured soil cohesion between 0.1 and 1.0 kPa and a bulk density of about 1.5 g cm^{-3}. Penetrometer measurements obtained by Luna 13 yielded comparable bearing-strength values. Apollo core samples reached depths of about 3 m and revealed stratified regolith layers comparable to the approximately 2 m core recovered by Luna 24 (Carrier 1974).

Analysis of roughly 382 kg of material returned by the Apollo missions revealed the composition and radiometric ages of lunar rocks, supporting the lunar magma ocean hypothesis and providing a detailed timeline of volcanic activity. Meanwhile, the Soviet Luna program (Luna 16, 20, and 24) returned samples from areas beyond the Apollo landing sites. Apollo orbiters used X-ray and gamma-ray spectrometers to map the Moon's global surface composition, while early Soviet orbital experiments primarily measured integral gamma-radiation levels (Vinogradov et al. 1966).

Table 2. Luna vs. Apollo: Side-by-side lunar observations and interpretations

Observation	Mission	Values / Observations	References
Mare basalt Titanium content	Luna	Low-Ti basalts: 1–3.4 wt% TiO_2	Luna 16/24; Heiken et al. (1991); Kocharov & Viktorov (1974); Jolliff et al. (2000)
	Apollo	High-Ti basalts: 6–13 wt% TiO_2	Apollo 11/17; Snyder et al. (1992)
Regolith density	Luna	Surface: 0.8 ± 0.1 g/cm^3 at 1–5 cm / Depth: ~1.2 g/cm^3 at 35 cm	Luna 13; Cherkasov et al. (1968)
	Apollo	Surface: 1.3 ± 0.2 g/cm^3 1–15 cm / Depth: 1.5–1.6 g/cm^3 at 30–60 cm	Apollo deep drill cores; Carrier et al. (1991)
Magnetic fields	Luna	Strong local anomalies: 20–30 nT at meter scale (Le Monnier)	Lunokhod 2 traverses; Dolginov et al. (1977)
	Apollo	Weak orbital fields: < 1 nT; surface varies: Apollo 12 ~37 nT, Apollo 15 ~4.5 nT, Apollo 16 ~232 nT	Hood et al. (1979)
Dust/horizon glow	Luna	Natural motion: 10%–20% sky brightness enhancement	Lunokhod 2; Severny et al. (1975)
	Apollo	Dust mobilized by astronauts	Apollo LEAM; Rennilson & Criswell (1974).

LEAM, Lunar Ejecta and Meteorites experiment.

Seismic activity was recorded by the Lunar Surface Experiments Package using passive instruments. The data indicated a deep structural layer and a fluid outer core (Williams et al. 2001). Heat flow probes measured subsurface temperature gradients and thermal conductivity of the regolith. Magnetometers on Lunokhod rovers detected local variations in the lunar magnetic field (Dolginov et al. 1977). Laser reflectors deployed by Apollo crews and mounted on Lunokhod enabled high precision measurements of lunar rotation and orbital motion (Williams et al. 2001).

Apollo astronauts directly associated collected samples with local stratigraphy (Wilhelms 1987). Soviet Luna landers and rovers captured extensive surface images, even though less detail on individual rock and soil layers were present. Pre-landing imagery from the Lunar Orbiter program helped with the mission planning and geological interpretation (Bowker & Hughes 1971). Instruments on Apollo recorded the solar wind, the lunar exosphere, and dust movement driven by electrostatic forces (Rennilson & Criswell 1974).

4. IMPLICATIONS FOR LUNAR SCIENCE AND MODERN RESEARCH

Chemical measurements of lunar soil collected during Apollo and Luna missions show similar overall composition at different landing areas. Physical characteristics of the surface soil still change from place to place because the lunar surface itself is not uniform. Measurements also depend on where the spacecraft landed and on the instruments used, since each experiment sampled only a small area compared with the surrounding region. Differences in titanium levels within mare basalts point to more than one volcanic source (Jolliff et al. 2000). Changes in regolith texture and structure are also related to surface slope and the long history of meteorite impacts that have reworked the lunar surface (Carrier et al. 1991).

Multiple space agencies are planning a new generation of lunar surface missions. Landing site selection explicitly targets scientific questions inherited from the Apollo and Luna era. Upcoming robotic and crewed missions will extend exploration into terrains largely bypassed during the first era of lunar activity, including the lunar far side, the South Pole–Aitken basin, and the polar highlands.

The Luna Program resumed after a long hiatus with the launch of Luna 25 in August 2023 and continues to focus on the lunar south polar region. The mission objectives include investigation of water ice and other volatile components in polar environments, while selecting terrain that allows safe landing conditions and adequate illumination (Turchinskaya & Slyuta 2024). The Luna 25 mission ended on 19 August 2023 when the spacecraft impacted the southwest rim of Pontécoulant G crater at 57.865°S, 61.360°E. Following the loss, Roscosmos redirected efforts toward the planned Luna 26 orbiter and Luna 27 lander (Turchinskaya & Slyuta 2024). The original landing site for Luna 25 was located north of Boguslawsky crater at 69.55°S, 43.54°E, with a backup location southwest of Manzinus crater (Krasilnikov et al. 2022; Turchinskaya & Slyuta 2024).

Future Russian lunar missions continue to focus on the south polar region, where Luna 27 is planned to land as close to the pole as practical. Site selection considers several practical factors, including safe terrain for landing, stable communication with Earth, and adequate sunlight for power (Turchinskaya & Slyuta 2024). Several landing ellipses have been studied, and Ellipses 1, 6, 13, and 16 are often discussed because geological interpretation suggests that material from the South Pole Aitken Basin may be present in those areas (Krasilnikov et al. 2022).

Terrain near the Boguslawsky and Boussingault craters contains Ellipses 6, 13, and 16, which lie on relatively smooth ground with gentle surface relief. Conditions there are considered safer than nearby heavily cratered terrain. Another possible landing area lies close to the Manzinus and Schomberger craters, where Ellipse 1 has also been identified as a high priority location (Krasilnikov et al. 2022).

Final selection depends on both scientific goals and engineering limits. One scientific aim involves studying physical, mechanical, and thermophysical properties of lunar soil at depths of about one to two meters, which favors places where volatile bearing material might occur (Turchinskaya & Slyuta 2024). Engineering constraints include sufficient solar illumination, generally above 35 percent, with several candidate ellipses reaching about 47 to 56 percent and Sites No. 1 and No. 2 reaching 55 and 56 percent (Turchinskaya & Slyuta 2024). Communication requirements demand Earth visibility greater than 50 percent. Terrain conditions must also include relatively low slopes, ideally below 7 to 10 degrees, together with low crater density to support safe landing operations (Krasilnikov et al. 2022; Turchinskaya & Slyuta 2024).

Recent assessments suggest that Russia's broader space program, including the Luna Program, has experienced delays and may be entering a period of reduced activity, with increasing attention directed toward the planned Russian Orbital Service Station (ROSS) (Vidal & Privalov 2024). Although Luna 26 and Luna 27 remain planned as an orbiter and lander, launch dates and the future direction of the program remain uncertain (Turchinskaya & Slyuta 2024; Vidal & Privalov 2024).

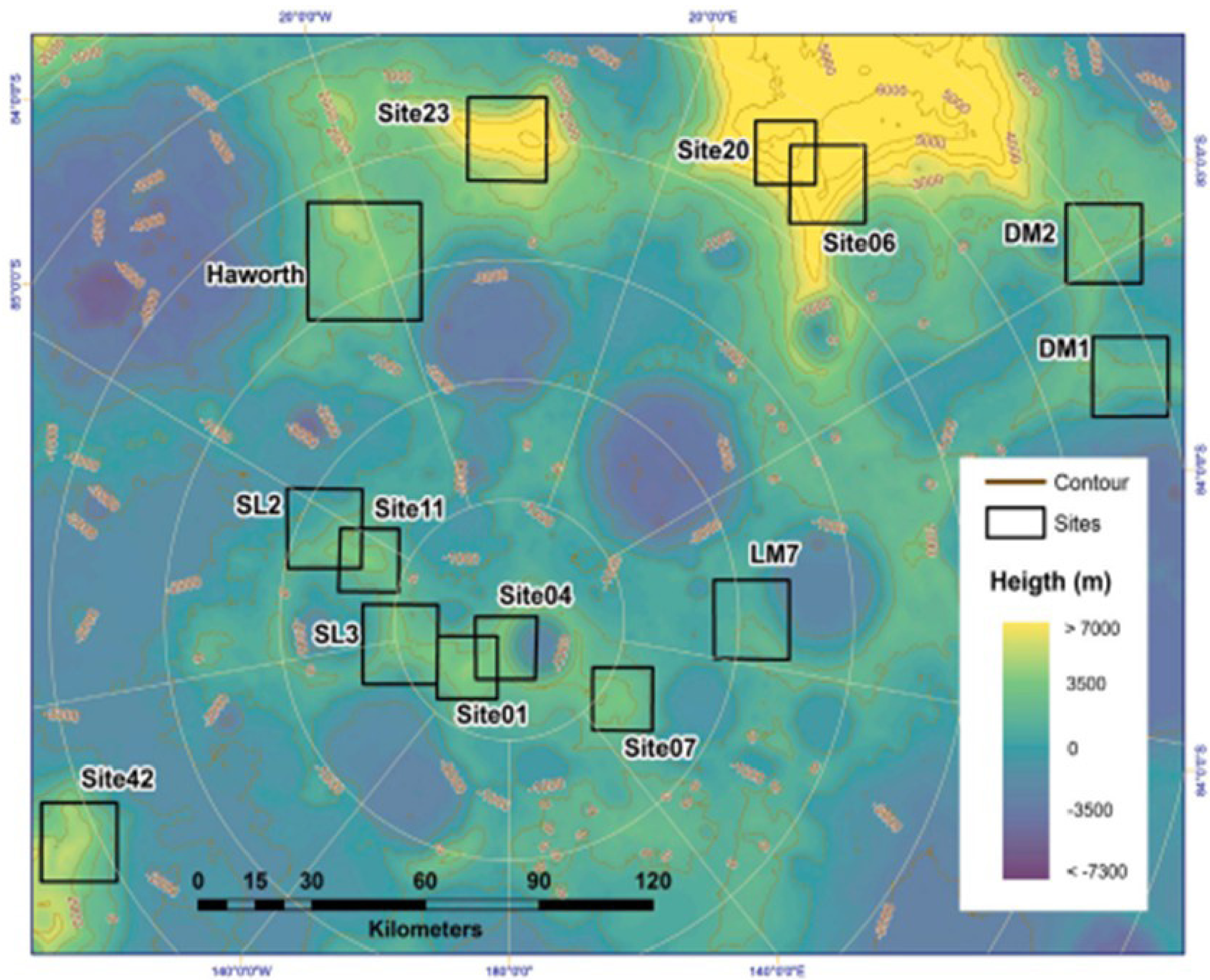

Fig. 13. Map illustrating the 13 candidate landing regions identified for the Artemis III mission, including Site 004. Each candidate region spans approximately 15 × 15 km. Topographic contours are shown at 1 km elevation intervals, and concentric circles denote 1° increments in latitude. Adapted from Peña-Asensio et al. (2025) with permission of author.

Within this international context, NASA's Artemis program is the main initiative for crewed lunar exploration. Artemis III is scheduled for the lunar south pole (see Fig. 13), while Apollo missions targeted equatorial sites to maintain direct communication with Earth. The south pole has permanently shadowed regions with water ice that could support longer surface work, local fuel production, and study of trapped volatiles (Peña-Asensio et al. 2025).

Candidate landing sites for Artemis III, within 6° of the south poles, were selected based on Apollo and Luna data. Priorities include reaching volatile deposits, sampling ancient anorthositic crust, and studying polar impact processes. The area has uneven terrain with slopes and obstacles that may affect surface operations.

Site selection also considers safe landing, direct Earth communication, sufficient solar power, equipment temperature limits, and maximizing scientific value (Peña-Asensio et al. 2025).

- Authors' analysis for Site 004: Using bearing strength measurements from Luna 24 (0.3–0.7 MPa) and wheel sinkage data from Lunokhod 2 (Basilevsky et al. 2021), we estimate that a lander footpad at Site 004 would sink 2–5 cm upon landing. Surface roughness (RMS slope) derived from Lunar Reconnaissance Orbiter Camera (LROC) topography at this site is ~8°, which is comparable to the Luna 24 landing area and acceptable for safe touchdown. These estimates confirm the mechanical suitability of Site 004 for Artemis III.
- Authors' analysis for Artemis: The Luna 24 core (Vinogradov 1971, Fig. 14) shows that lunar regolith

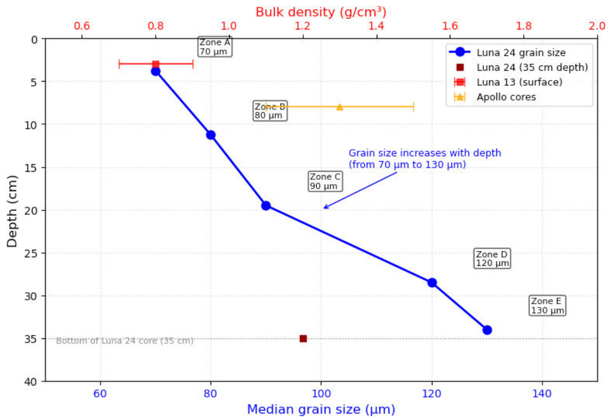

Fig. 14. Median grain size increase with depth in the Luna 24 core, based on the five stratigraphic zones (A through E). Grain size increases from 70 µm in Zone A (5.5 cm depth) to 130 µm in Zone E (35 cm depth). This depth-dependent coarsening indicates progressively higher soil strength, which has direct implications for the design of drills for future missions such as Artemis. Data from Vinogradov (1971).

becomes coarser with depth – median grain size increases from ~70 µm near the surface to ~130 µm at 35 cm depth (Fig. 14). For any Artemis drill, this means the tool must handle increasing grain size and likely increasing soil strength. A variable penetration rate would prevent the overload problem that terminated Luna 24 drilling prematurely (Heiken et al. 1991).

5. CONCLUSION

The Luna Program showed that systematic robotic exploration could accomplish complex scientific objectives. Between 1958 and 1976 it progressed from simple impactors to rovers and automated sample-return spacecraft. Operational techniques such as remote rover control with communication delays, automated drilling, and sealed sample containment demonstrated that complex surface operations could be carried out without human presence. Surface experiments also provided important constraints for landing and scientific analysis. Penetrometer measurements and mechanical tests from Lunokhod 2 established near-surface density and bearing strength capable of supporting landed vehicles. The RIFMA X-ray fluorescence traverses from Lunokhod 2 revealed compositional gradients across mare–highland boundaries rather than sharp contacts. Sample-return missions, Luna 16, Luna 20, and Luna 24, returned representative materials including low-titanium mare basalts, anorthositic highland samples, and a two-meter stratified core that anchors interpretations of lunar stratigraphy and regolith evolution. Additional results, including localized magnetic anomalies near impact structures, laser-ranging reflectors, and other geophysical observations, have provided constraints on models of lunar crustal structure and interior processes.

Results from the Luna Program remain an important reference for current lunar research and mission planning. Measurements of regolith properties and surface conditions are used to define landing constraints and to interpret orbital data from missions such as the Lunar Reconnaissance Orbiter and Chandrayaan-1. Future missions, including Luna-26, Luna-27, and the Artemis Program, will build on earlier measurements and operational experience when planning robotic and human exploration of the Moon. Knowledge gained from these missions continues to support both crewed and uncrewed exploration and contributes to a better understanding of lunar surface processes and the lunar environment.

ACKNOWLEDGEMENT

This research was supported by the Global-Learning & Academic Research Institution for Master's, PhD Students, and Postdocs (G-LAMP) Program of the National Research Foundation of Korea (NRF), funded by the Ministry of Education (No. RS-2025-25442707).

ORCIDs

Ulkar Karimova https://orcid.org/0000-0003-3396-2815
Yu Yi https://orcid.org/0000-0001-9348-454X
Kyungguk Min https://orcid.org/0000-0002-2095-8529

REFERENCES

Basilevsky AT, On the evolution rate of small lunar craters, Proceedings of the 7th Lunar Science Conference, Moscow, USSR, 4-8 Jun 1974.

Basilevsky AT, Lunokhod-2: a retrospective, Sol. Syst. Res. 55, 289-306 (2021).

Basilevsky AT, Abdrakhimov AM, Head JW, Pieters CM, Wu Y, et al., Geologic characteristics of the Luna 17/Lunokhod 1 and Chang'E-3/Yutu landing sites, Northwest Mare Imbrium of the Moon, Planet. Space Sci. 117, 385-400 (2015). https://doi.org/10.1016/j.pss.2015.08.006

Basilevsky AT, Malenkov MI, Volov VA, Abdrakhimov AM, Kozlova NA, et al., Estimation of the strength of the lunar soil by the depth of the lunar rover wheel tracks, Sol.

Syst. Res. 55, 285-308 (2021). https://doi.org/10.1134/S0038094621040018

Bowker DE, Hughes JK, Lunar Orbiter Photographic Atlas of the Moon, Report No. NASA SP-206 (1971).

Carrier WD III, Apollo drill core depth relationships, Moon. 10, 183-194 (1974). https://doi.org/10.1007/BF00655719

Carrier WD III, Olhoeft GR, Mendell W, Physical properties of the lunar surface, in Lunar Sourcebook: A User's Guide to the Moon, eds. Heiken GH, Vaniman DT, French BM (Cambridge Univ. Press, Cambridge, 1991), 475-594.

Cherkasov II, Mikheev VV, Smorodinov MI, Zobachev NM, Mikhailov IL, et al., Determination of the structural and mechanical properties of the lunar soil by the automatic lunar station "Luna-13", J. Eng. Phys. 14, 309-311 (1968). https://doi.org/10.1007/BF00828540

Chertok BE, Rockets and people: creating a rocket industry, vol. 2, NASA History Division, ed. Siddiqi AA (NASA, Washington, 2006).

Christensen EM, Choate R, Jaffe LD, Spencer RL, Sperling FB, et al., Surveyor V: lunar surface mechanical properties, Science. 158, 637-640 (1967). https://doi.org/10.1126/science.158.3801.637

Dolginov SS, Yeroshenko YG, Zhuzgov LN, Sharova VA, Vnuchkov GA, et al., Magnetic field in Le Monnier Bay according to data of Lunokhod 2, Proceedings of the Soviet-American Conference on the Cosmochemistry of the Moon and Planets, Part 1 (NASA, Washington, 1977), 433-441.

Fong T, Abercromby A, Bualat MG, Deans MC, Hodges KV, et al., Assessment of robotic recon for human exploration of the Moon, Acta Astronaut. 67, 1176-1188 (2010). https://doi.org/10.1016/j.actaastro.2010.06.029

Gattacceca J, Boustie M, Hood L, Cuq-Lelandais JP, Fuller M, et al., Can the lunar crust be magnetized by shock: experimental groundtruth, Earth Planet. Sci. Lett. 299, 42-53 (2010). https://doi.org/10.1016/j.epsl.2010.08.011

Hall RC, Lunar Impact: A History of Project Ranger, NASA SP-4210 (NASA, Washington, 1977).

Hartzell CM, Dynamics of 2D electrostatic dust levitation at asteroids, Icarus. 333, 234–242 (2019). https://doi.org/10.1016/j.icarus.2019.05.013

Harvey B, Soviet and Russian Lunar Exploration (Praxis Publishing, Chichester, 2007).

Heiken GH, Vaniman DT, French BM, Lunar Sourcebook: A User's Guide to the Moon (Cambridge Univ. Press, Cambridge, 1991).

Hood LL, Coleman PJ Jr, Russell CT, Wilhelms DE, Lunar magnetic anomalies detected by the Apollo subsatellite magnetometers, Phys. Earth Planet. Inter. 20, 291-311 (1979). https://doi.org/10.1016/0031-9201(79)90052-9

Jolliff BL, Gillis JJ, Haskin LA, Korotev RL, Wieczorek MA, Major lunar crustal terranes: surface expressions and crust-mantle origins, J. Geophys. Res. Planets. 105, 4197-4216 (2000). https://doi.org/10.1029/1999JE001103

Karachevtseva I, Oberst J, Scholten F, Konopikhin A, Shingareva K, et al., Cartography of the Lunokhod-1 landing site and traverse from LRO image and stereo-topographic data, Planet. Space Sci. 85, 175-187 (2013). https://doi.org/10.1016/j.pss.2013.06.002

Kocharov GE, Viktorov SV, Chemical composition of lunar surface in the region of "Lunokhod-2" operation, Dokl. Akad. Nauk SSSR. 214, 71-74 (1974).

Kosofsky LJ, El-Baz F, The Moon as Viewed by Lunar Orbiter, NASA SP-200 (NASA, Washington, 1970).

Krasilnikov SS, Krasilnikov AS, Ivanov MA, Geological details of the main landing ellipses of Luna-25, Sol. Syst. Res. 56, 135-144 (2022). https://doi.org/10.1134/S0038094622020058

McKay DS, Heiken G, Basu A, Blanford G, Simon S, et al., The lunar regolith, in Lunar Sourcebook: A User's Guide to the Moon, eds. Heiken GH, Vaniman DT, French BM (Cambridge Univ. Press, Cambridge, 1991), 285-356.

Murphy TW Jr, Adelberger EG, Battat JBR, Hoyle CD, Johnson NH, et al., Laser ranging to the lost Lunokhod 1 reflector, Icarus. 211, 1103-1108 (2011). https://doi.org/10.1016/j.icarus.2010.11.010

NASA Scientific Visualization Studio, First photograph of the lunar far side returned by Luna 3 (1959) [Internet], viewed 2026 Mar 9, available from: https://science.nasa.gov/resource/first-photo-of-the-lunar-far-side/

NASA/JPL/Arizona State University, Surveyor 1 on the lunar surface (*Oceanus procellarum*) (2026) [Internet], viewed 2026 Mar 9, available from: https://photojournal.jpl.nasa.gov/

Ness NF, Behannon KW, Scearce CS, Cantarano SC, Early results from the magnetic field experiment on Lunar Explorer 35, J. Geophys. Res. 72, 5769-5778 (1967). https://doi.org/10.1029/JZ072i023p05769

Peña-Asensio E, Neira-Acosta ÁS, Sánchez-Lozano JM, Evaluating potential landing sites for the Artemis III mission using a multi-criteria decision making approach, Acta Astronaut. 226, 469-478 (2025). https://doi.org/10.1016/j.actaastro.2024.10.049

Pieters CM, Goswami JN, Clark RN, Annadurai M, Boardman J, et al., Character and spatial distribution of OH/H_2O on the surface of the Moon seen by M^3 on Chandrayaan-1, Science. 326, 568-572 (2009). https://doi.org/10.1126/science.1178658

Rennilson JJ, Criswell DR, Surveyor observations of lunar horizon-glow, Moon. 10, 121-142 (1974). https://doi.org/10.1007/BF00655715

Severny AB, Terez EI, Zvereva AM, The measurements of sky brightness on Lunokhod-2, The Moon, 14, 123-128 (1975). https://doi.org/10.1007/BF00562978

Siddiqi AA, Challenge to Apollo: The Soviet Union and the Space Race, 1945-1974, NASA SP-2000-4408 (NASA History Division, Washington, 2000).

Snyder GA, Taylor LA, Neal CR, A chemical model for generating the sources of mare basalts: combined equilibrium and fractional crystallization of the lunar magmasphere, Geochim. Cosmochim. Acta. 56, 3809-3823 (1992). https://doi.org/10.1016/0016-7037(92)90172-F

Song YJ, Bang J, Bae J, Hong S, Lunar orbit acquisition of the Korea Pathfinder lunar orbiter: design reference vs actual flight results, Acta Astronaut. 213, 336-343 (2023). https://doi.org/10.1016/j.actaastro.2023.09.021

Szalay JR, Pokorný P, Sternovsky Z, Kupihar Z, Poppe AR, et al., Impact ejecta and gardening in the lunar polar regions, J. Geophys. Res. Planets. 124, 143-154 (2019). https://doi.org/10.1029/2018JE005756

Turchinskaya OI, Slyuta EN, Landing site choice for Luna-27 mission in the Moon South Polar Region, Acta Astronaut. 222, 346-358 (2024). https://doi.org/10.1016/j.actaastro.2024.06.011

Vidal F, Privalov R, Russia in outer space: a shrinking space power in the era of global change, Space Policy. 69, 101579 (2024). https://doi.org/10.1016/j.spacepol.2023.101579

Vinogradov AP, Preliminary data on lunar ground brought to Earth by automatic probe "Luna-16," Proceedings of the Second Lunar Science Conference, ed. Levinson AA (MIT Press, Cambridge, 1971).

Vinogradov AP, Surkov YA, Chernov GM, Kirnozov FF, Nazarkina GS, Measurements of Gamma-radiation of the Lunar Surface on the Space Station Luna-10, NASA GSFC Technical Report, ST-LPS-ACH-10-517 (1966).

Weber RC, Lin PY, Garnero EJ, Williams Q, Lognonné P, Seismic detection of the lunar core, Science. 331, 309-312 (2011). https://doi.org/10.1126/science.1199375

Wilhelms DE, McCauley JF, Trask NJ, The Geologic History of the Moon: U.S. Geological Survey Professional Paper 1348 (U.S. Government Printing Office, Washington, 1987).

Williams JG, Boggs DH, Yoder CF, Ratcliff JT, Dickey JO, Lunar rotational dissipation in solid body and molten core, J. Geophys. Res. Planets. 106, 27933-27968 (2001). https://doi.org/10.1029/2000JE001396

Zuber MT, Smith DE, Neumann GA, Goossens S, Andrews-Hanna JC, et al., Gravity field of the Orientale basin from the Gravity Recovery and Interior Laboratory mission, Science. 354, 438-441 (2016). https://doi.org/10.1126/science.aag0519